photonics

Article

Single-Path Spatial Polarization Modulation for Vector Transmission Matrix Measurement and Polarization Control in Scattering Media

Edvard Grigoryan , Aram Sargsyan , Tatevik Sarukhanyan * and Mushegh Rafayelyan

PhotonicsAI Lab, Center for Optics and Photonics, Institute of Physics, Yerevan State University, Yerevan 0025, Armenia; edvard.grigoryan1@edu.ysu.am (E.G.); aramsargsyan@ysu.am (A.S.); mushegh.rafayelyan@ysu.am (M.R.)

* Correspondence: tatevik.sarukhanyan@ysu.am

Abstract

Controlling light's polarization through disordered media is crucial for advanced optical applications but remains challenging due to scattering and depolarization. Most existing approaches either require interferometric or multi-path measurements, or they recover only part of the polarization response. We present a comprehensive approach for spatially resolved polarization control by accurately retrieving the vector transmission matrix (VTM) of a scattering system from intensity-only, full-Stokes polarimetric measurements. Using a simple single-path setup comprising a liquid-crystal spatial light modulator (SLM) with a tunable retarder after it, we achieve spatial polarization modulation at the input, thereby enabling probing of the medium's polarization–scattering characteristics. The VTM is retrieved with an adapted Gerchberg–Saxton procedure that enforces not only the measured output amplitudes but also the relative phase between the two orthogonal output polarization components obtained from the Stokes parameters. We show that a single retarder setting results in inter-block correlations in the retrieved VTM due to input coupling, while two linearly independent retarder settings decouple the intrinsic blocks and recover the full VTM. In our experiment, for a 16×16 set of input–output spatial modes, the VTM is retrieved with about 90% accuracy, enabling polarization-resolved focusing with up to $10\times$ enhancement for horizontal, vertical, arbitrary linear, and circular states. This work offers a compact framework for active polarization shaping and for polarimetric characterization of complex media, advancing our understanding of vectorial light–matter interactions.

Keywords: vector transmission matrix; spatial polarization modulation; scattering media; full-Stokes polarimetry; spatial light modulator; Gerchberg–Saxton algorithm

check for updates

Received: 16 October 2025
Revised: 4 November 2025
Accepted: 13 November 2025
Published: 20 November 2025

Citation: Grigoryan, E.; Sargsyan, A.; Sarukhanyan, T.; Rafayelyan, M. Single-Path Spatial Polarization Modulation for Vector Transmission Matrix Measurement and Polarization Control in Scattering Media. *Photonics* **2025**, *12*, 1145. https://doi.org/10.3390/photonics12111145

1. Introduction

The propagation of light through inhomogeneous and disordered media, such as biological tissues, atmospheric turbulence, turbid water, or multimode fibers, presents a significant challenge to optical control and imaging [1–8]. As light traverses such media, its wavefront undergoes severe distortions, leading to the formation of complex and seemingly random speckle patterns [9,10]. Beyond spatial mixing, multiple scattering events also profoundly alter the polarization state of the incident light, leading to depolarization and a loss of correlation with the original polarization state [11]. This complex interplay between spatial and polarization degrees of freedom for a static medium is deterministic, showing that apparently random media can be learned or measured and then actively inverted, transforming them into programmable optical elements [12].

The early phase of the field established scalar control. By optimizing or measuring the field at a target point, light can be refocused through opaque slabs, its arrival time and spectrum can be tailored, and complex media can be repurposed as lenses or spectral filters [13–18]. Transmission-matrix methods then showed that the linear operator linking input modes to output modes can be measured once and reused to synthesize many different targets without re-optimization [19]. This created a practical toolbox for deterministic wave control.

Polarization adds an essential dimension. Many light–matter interactions are polarization selective, polarization can serve as an information channel for multiplexing, and polarimetry itself is a sensitive probe of structure in materials and tissues. Extending wavefront shaping into this vectorial regime followed two complementary paths. On the adaptive side, a phase-only modulation of the linearly polarized input can lead to the full control of output polarization behind a multiple-scattering medium by leveraging native coupling between spatial and polarization degrees of freedom [20,21]. Polarization was also used directly as a control variable for focusing through turbid media [22]. On the model-based side, the community extended transmission-matrix thinking toward polarization degree of freedom by reconstructing vector maps that link the two orthogonal polarization components of input to the two output components, often referred to as the vector transmission matrix (VTM). In that approach, one first measures the full [12,23] or partial [24] VTM and then uses it to predict polarization-resolved outputs anywhere in the field of view and to synthesize desired polarization states with a single linear solve. The illumination bandwidth provides another degree of freedom; under broadband excitation, path-length selection can produce a polarization-memory effect that passively assists polarization recovery and modifies the effective vector mapping [25].

Despite substantial progress, there is still a need for robust, experimentally accessible methods that combine comprehensive vector characterization with practical implementation. The challenge is to develop systems that not only achieve arbitrary polarization control but also provide a clear, deterministic understanding of the underlying vector light–matter interactions—without complex or sensitive multi-path interferometric setups and without relying solely on adaptive “black-box” optimization.

In this work we present a simple, single-path method to retrieve the VTM from intensity-only, full-Stokes measurements and to use it for spatially resolved polarization control in scattering media. The setup consists of a liquid-crystal SLM followed by a tunable retarder that sets the input polarization pattern, and a full-Stokes polarimetry module (FSPM) at detection. We adapt the well-known Gerchberg–Saxton (GS) algorithm for transmission-matrix retrieval [26] to enforce both the output magnitudes and the relative phase between the orthogonal output polarization components provided by the FSPM, so no interferometer or split-beam optics are required. With a single retarder setting, the two orthogonal input components are optically coupled and the retrieved VTM shows inter-block correlations. Using two linearly independent retardance settings separates the intrinsic blocks and recovers the full VTM. After measuring the VTM with two retardances, we use this calibrated model for inverse design by computing SLM phase patterns that produce arbitrary target locations and polarization states at the output. Overall, the method keeps the hardware simple while enabling both polarization shaping and polarimetric characterization of complex media, including the generation of horizontal, vertical, arbitrary linear, and circular states at selected locations.

2. Experimental Setup

A common single-path scattering setup comprises a liquid-crystal SLM for input wavefront modulation, an electrically tunable liquid-crystal variable retarder (LCVR) that maps this phase into spatial polarization modulation, a strongly scattering sample that scrambles both spatial and polarization degrees of freedom, and an FSPM at detection (Figure 1). A linearly polarized, single-frequency laser at $\lambda = 532\,\mathrm{nm}$ is converted to right-circular polarization (RCP) by a quarter-wave plate (QWP) at 45°, then expanded (BE) to match the SLM aperture. The beam passes through a beam splitter (BS) to the reflective, liquid-crystal SLM, acquires the programmed phase, and is redirected by the BS toward the sample arm.

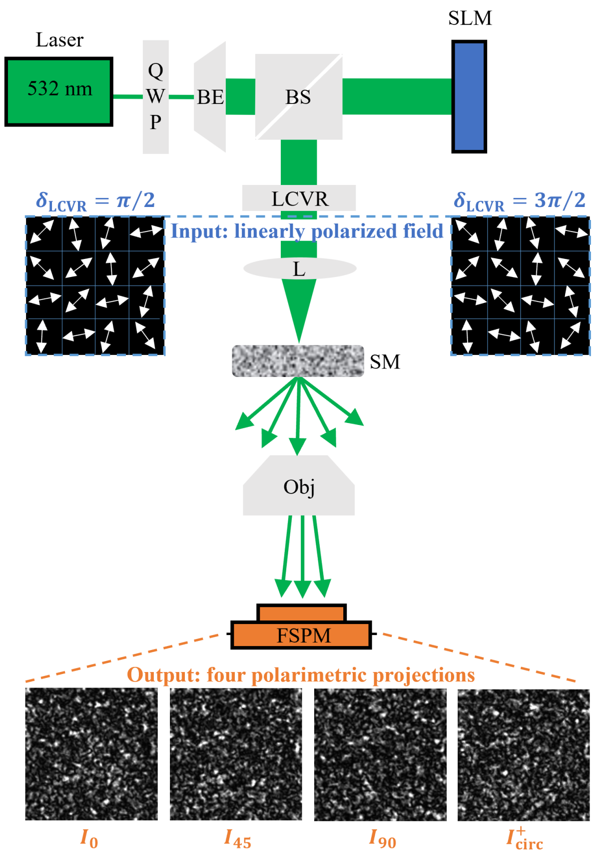

Figure 1. Experimental setup and polarimetric acquisition. A 532 nm laser beam is initially converted to right-circular polarization by a QWP at 45°, then expanded (BE), and directed by a beam splitter (BS) to a reflective, liquid-crystal SLM. After reflection, an LCVR with its fast axis fixed at −45° applies a selectable retardance δ; two settings used here are $\pi/2$ and $3\pi/2$ (blue dashed insets). For each setting, the SLM phase $\phi(\mathbf{r})$ is converted into a spatially varying, linearly polarized input field (the AoLP map flips sign between the two cases). A relay lens (L) illuminates the scattering medium (SM), and an objective (Obj) images the transmitted speckle onto a full-Stokes polarimetry module (FSPM). The FSPM records four analyzer images I_0, I_{45}, I_{90}, and $I^{(+)}_{\mathrm{circ}}$, enabling per-pixel full-Stokes polarimetry.

Immediately after the BS, a computer-controlled LCVR with its fast axis fixed at −45° applies two retardances, $\delta = \pi/2$ and $\delta = 3\pi/2$. These settings produce two linearly independent spatial polarization modulations from the same SLM phase pattern (see Appendix A), which we later use for the full retrieval of the system VTM. A relay lens (L, $f = 100\,\mathrm{cm}$) focuses the beam onto a 1 mm PTFE (Teflon) scattering medium (SM), and a collection objective (Obj) images the transmitted speckle onto the FSPM. In this configuration, a 1 mm PTFE slab is sufficient to generate a fully developed speckle pattern, and the use of a single-frequency laser is essential to obtain a high-contrast speckle field.

The FSPM combines a polarization camera with an LCVR to acquire four analyzer images per cycle: I_0 (analyzer along x), I_{90} (along y), I_{45} (45°), and $I_{\mathrm{circ}}^{(+)}$ (corresponding to right-circularly polarized projection). To obtain these measurements, the LCVR is alternately set to 0 and $\pi/4$ retardance. The zero-retardance state enables capture of the three linear polarization components I_0, I_{90}, and I_{45}, while the $\pi/4$ state, combined with an analyzer at 0°, provides the circular component $I_{\mathrm{circ}}^{(+)}$. The intensities along different directions are captured simultaneously by means of a pixelated polarization filter array on the polarization camera. These four frames uniquely determine the Stokes parameters per pixel via $S_0 = I_0 + I_{90}$, $S_1 = I_0 - I_{90}$, $S_2 = 2I_{45} - S_0$, and $S_3 = 2I_{\mathrm{circ}}^{(+)} - S_0$, which provide $|E_x|$, $|E_y|$, and the relative phase $\Delta\phi = \mathrm{atan2}(S_3, S_2)$ used as constraints in the VTM retrieval. To ensure accurate measurements, essential alignment of the FSPM was performed (see Appendix C).

The pixelated architecture of the polarization camera means that the four linear projections (0°, 45°, 90°, 135°) are sampled at slightly different sensor locations. To ensure that the Stokes parameters refer to the same physical area, we do not use individual sensor pixels directly. Instead, we define output macropixels of size 8×8 sensor pixels (chosen to be comparable to the speckle grain size) and, for each macropixel, we average separately all pixels of a given analyzer orientation (0°, 45°, 90°, 135°). The four averaged intensities are then used to compute the Stokes parameters for that macropixel. This procedure removes the subpixel misregistration between analyzer spatial channels and improves the signal-to-noise ratio. More details on the technical specifications of the optical equipment can be found in Appendix C.

3. VTM Retrieval and Measurement Procedure

We describe the scattering medium by a $2m \times 2n$ VTM

$$T = \begin{bmatrix} T_{xx} & T_{xy} \\ T_{yx} & T_{yy} \end{bmatrix}, \qquad \begin{bmatrix} \mathbf{E}_{\mathrm{out},x} \\ \mathbf{E}_{\mathrm{out},y} \end{bmatrix} = \begin{bmatrix} T_{xx} & T_{xy} \\ T_{yx} & T_{yy} \end{bmatrix} \begin{bmatrix} \mathbf{E}_{\mathrm{in},x} \\ \mathbf{E}_{\mathrm{in},y} \end{bmatrix}, \tag{1}$$

where $\mathbf{E}_{\mathrm{out},x}$ and $\mathbf{E}_{\mathrm{out},y}$ denote the complex amplitudes of the output field projected onto a fixed orthogonal linear polarization basis (horizontal x and vertical y) corresponding input light field components in the same basis. Bold symbols denote stacked vectors over the n input pixels and m output pixels.

For any fixed retardance δ of the LCVR, the input components obey a pixelwise affine relation $\mathbf{E}_{\mathrm{in},y} = \alpha(\delta)\,\mathbf{E}_{\mathrm{in},x} + \mathbf{g}(\delta)$ (derivation in Appendix B). Consequently, a single δ yields only the effective superpositions $A(\delta) = T_{xx} + \alpha(\delta)T_{xy}$ and $C(\delta) = T_{yx} + \alpha(\delta)T_{yy}$, along with their respective offset terms. This constitutes a $2m \times n$ mapping restricted to that coupled-input subspace, meaning the four intrinsic blocks are not uniquely determined. To recover the full VTM, two linearly independent retardances are sufficient. In this work we use $\delta = \pi/2$ and $\delta = 3\pi/2$; see Appendix B for details.

We then estimate T with an adapted Gerchberg–Saxton algorithm that uses the four FSPM images to impose, at each output pixel, the measured magnitudes $|E_x|, |E_y|$ and the relative phase $\Delta\phi$ (implementation available in our open-source code [27]). For probe inputs stacked columnwise in $E_{\mathrm{in}} \in \mathbb{C}^{2n \times k}$ (here k includes patterns measured at both LCVR retardances), a current estimate $T_{\mathrm{est}} \in \mathbb{C}^{2m \times 2n}$ predicts $E_{\mathrm{out}}^{\mathrm{pred}} = T_{\mathrm{est}} E_{\mathrm{in}}$. We then overwrite the predicted magnitudes and relative phase using the FSPM data: for each output pixel,

$$E_x^{\mathrm{upd}} = \sqrt{I_0}\, e^{\,i \arg\left(E_x^{\mathrm{pred}}\right)}, \qquad E_y^{\mathrm{upd}} = \sqrt{I_{90}}\, e^{\,i\left(\arg(E_x^{\mathrm{pred}})+\Delta\phi\right)}, \qquad \Delta\phi = \mathrm{atan2}(S_3, S_2),$$

and assemble $E_{\mathrm{out}}^{\mathrm{upd}} = \left[\, E_x^{\mathrm{upd}};\, E_y^{\mathrm{upd}} \,\right]$. Finally, an inverse transformation defines the new estimation of VTM

$$T_{\mathrm{est}} \;\leftarrow\; E_{\mathrm{out}}^{\mathrm{upd}}\, E_{\mathrm{in}}^{\dagger}.$$

Iterations are repeated until either convergence is reached or a maximum number of iterations is exceeded. Following the criterion used in [26], we declare convergence when the correlation between the VTM estimate at iteration i and the one at iteration $i-2$ exceeds $1-10^{-6}$. As a correlation metric we use the absolute value of the Complex Pearson Correlation Coefficient (CPCC) [28] computed on the vectorized (flattened) forms of the two matrices. The block diagram in Figure 2 summarizes the steps.

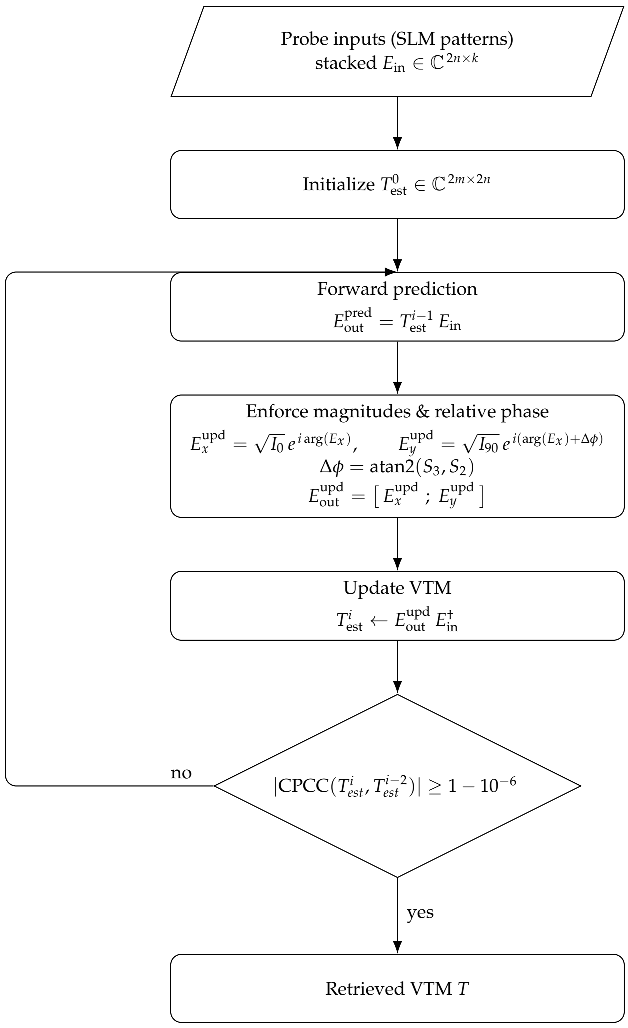

Figure 2. Adapted GS retrieval. Each iteration predicts $E_{\mathrm{out}}^{\mathrm{pred}}$, enforces magnitudes and relative phase to form $E_{\mathrm{out}}^{\mathrm{upd}} = \left[\, E_x^{\mathrm{upd}};\, E_y^{\mathrm{upd}} \,\right]$, and updates the VTM via $T_{\mathrm{est}} \leftarrow E_{\mathrm{out}}^{\mathrm{upd}}\, E_{\mathrm{in}}^{\dagger}$.

4. Experimental Results and Polarization Control

We retrieve the full $2m \times 2n$ vector transmission matrix T with the adapted GS algorithm in two acquisition modes: (i) a single LCVR retardance $\delta = \pi/2$ and (ii) dual retardances $\delta \in \{\pi/2, 3\pi/2\}$. In both cases we use $k = 5000$ probe inputs with $n = 16$ input pixels and record $m = 16$ output pixels.

Figure 3 shows, for the single-retardance case, the magnitude and phase of the retrieved VTM. As expected from the input coupling (Appendix B), the four blocks display visible similarities. To quantify this, we processed the matrix as in Popoff et al. [19]: we removed the reference-amplitude contribution, applied the same spatial decimation to reduce nearest-neighbor correlations, and then computed the singular values of the resulting matrices. The singular values are the nonnegative values obtained from the singular value decomposition (SVD) and provide a compact way to compare a measured matrix with a random-matrix prediction. The corresponding curves in Figure 3 are plotted as normalized histograms and are shown together with the quarter-circle law, i.e., the expected singular-value distribution for a complex random matrix with the same aspect ratio and i.i.d. (independent and identically distributed) entries [29]. While each block separately is close to this law, the singular-value distribution of the full VTM deviates from it, which indicates residual correlations between blocks introduced by using only one retardance. Each curve is averaged over 64 disorder realizations and VTM retrievals. We also calculate the correlation between the output intensities obtained experimentally and those calculated using the retrieved VTM for a set of test inputs generated in the single-retardance mode and not included in the optimization process. On average, we observe about 90% correlation between the measured and calculated intensities. This level of agreement is consistent with the fact that the GS-type retrieval can converge to a local minimum for this coupled-input configuration, but it can also be limited by nonideal circular-polarization preparation at the SLM input, polarization changes introduced by intermediate optics (beam expander, beam splitter, relay lens, objective), and environmental noise such as mechanical vibrations and slow thermal drifts in the setup. Nevertheless, we consider the experimental results satisfactory, as similar levels of performance have been reported in other studies addressing comparable problems and using similar algorithmic approaches [30,31]

Repeating the retrieval with two independent LCVR retardance settings decouples the intrinsic blocks of the VTM. Figure 4 shows the magnitude and phase of the resulting VTM retrieved by the adapted GS algorithm, which no longer display visual or statistical similarities between the four sub-blocks. Applying the same singular value distribution analysis as before shows that the distributions of each block and of the full VTM closely follow the quarter-cricle low, see Figure 4 . This clear contrast with the single-retardance case confirms that introducing a second, linearly independent retardance effectively removes artificial inter-block correlations and yields a fully decorrelated complex random VTM. The curves are averaged over 64 independent VTM measurements corresponding to different disorder realizations. Moreover, correlations of the output intensities on a test set generated in the dual-retardance mode show a performance similar to the previous setting, with an average correlation of approximately 90%.

Notably, to illustrate the robustness of the adapted GS retrieval algorithm, we performed a statistical analysis of its performance over 64 independent experiments, each yielding a distinct transmission matrix; see Appendix D.

Finally, we use the retrieved VTM $T \in \mathbb{C}^{2m \times 2n}$ to synthesize polarization-resolved foci at arbitrary output pixels. In practice we generate the SLM phase in a single shot with a shallow feed-forward neural network that approximates the phase-only projection implied by the forward model in Equation (1) and is trained to maximize the target-pixel intensity under a desired Stokes state (code and training details in [27]). Figure 5 shows five examples: four linear states ($0^\circ, 45^\circ, 90^\circ, 135^\circ$) and one left-circular state. For the linear cases, the images are rendered with hue encoding the AoLP and brightness proportional to intensity; for the circular case, the focus appears white in the AoLP rendering (locally random AoLP) and we report the DoLP in the text.

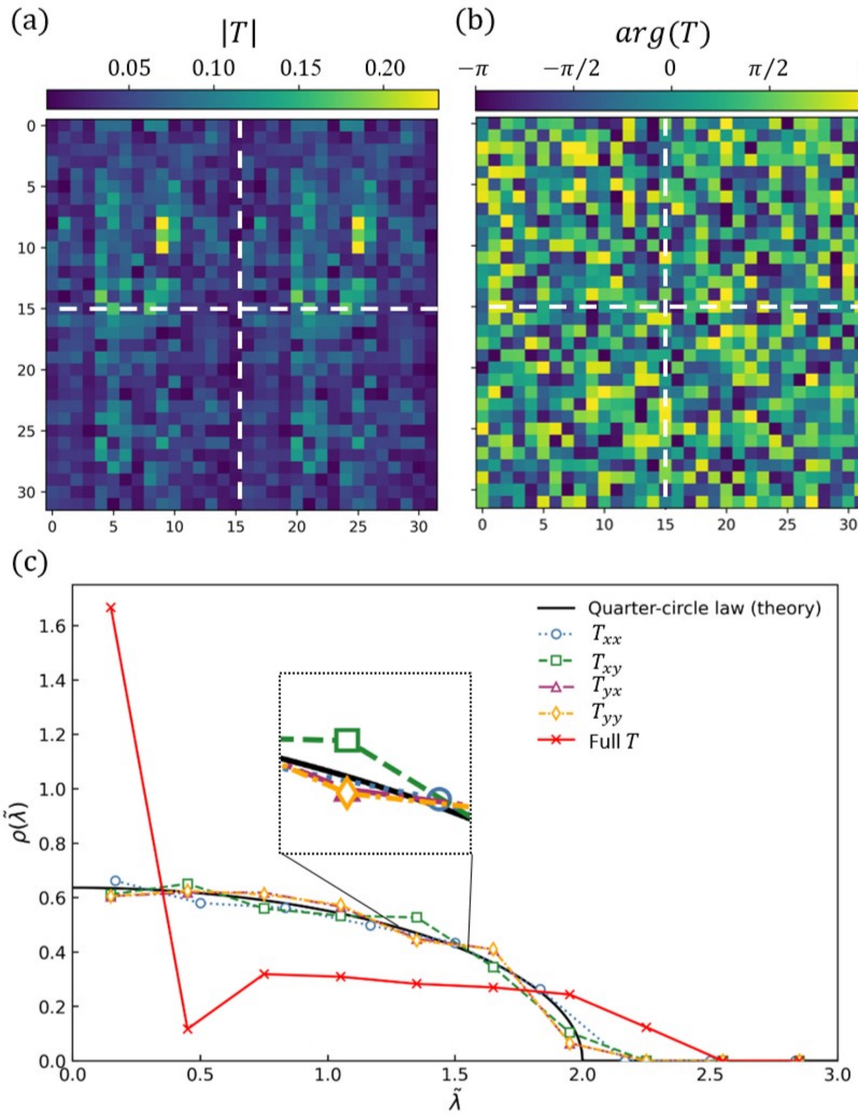

Figure 3. Single-retardance retrieval ($\delta = \pi/2$). (**a**) Magnitude and (**b**) phase of the retrieved $2m \times 2n$ VTM T. (**c**) Singular-value distributions of the four intrinsic blocks (T_{xx}, T_{xy}, T_{yx}, T_{yy}) and of the full matrix T after amplitude normalization and spatial decimation as in [19], shown together with the quarter-circle prediction for an i.i.d. complex random matrix [29]. The full matrix deviates from the quarter-circle law because of inter-block correlations, which are a direct consequence of the input coupling when only one retardance is used. An enlarged view of a selected region is provided for better visibility.

Quantitatively, the intensity enhancement at the target (peak intensity in a 64×64 ROI divided by the mean intensity of the surrounding (non-focusing) area after wavefront shaping) was $\eta_{0^\circ} = 8.9$, $\eta_{45^\circ} = 10.1$, $\eta_{90^\circ} = 8.3$, $\eta_{135^\circ} = 7.5$, and $\eta_{\mathrm{LCP}} = 7.1$. The polarization fidelity at the focus, averaged over the ROI, was $\mathrm{AoLP}_{0^\circ} = 0.8^\circ$ ($\sigma = 5.1^\circ$), $\mathrm{AoLP}_{45^\circ} = 45.2^\circ$ ($\sigma = 5.7^\circ$), $\mathrm{AoLP}_{90^\circ} = 89.9^\circ$ ($\sigma = 5.8^\circ$), $\mathrm{AoLP}_{135^\circ} = 134.1^\circ$ ($\sigma = 5.7^\circ$), and, for the circular target, $\mathrm{DoLP}_{\mathrm{LCP}} = 0.1$ ($\sigma = 0.02$), where σ denotes the standard deviation of the polarization angle or degree of polarization within the focal region.

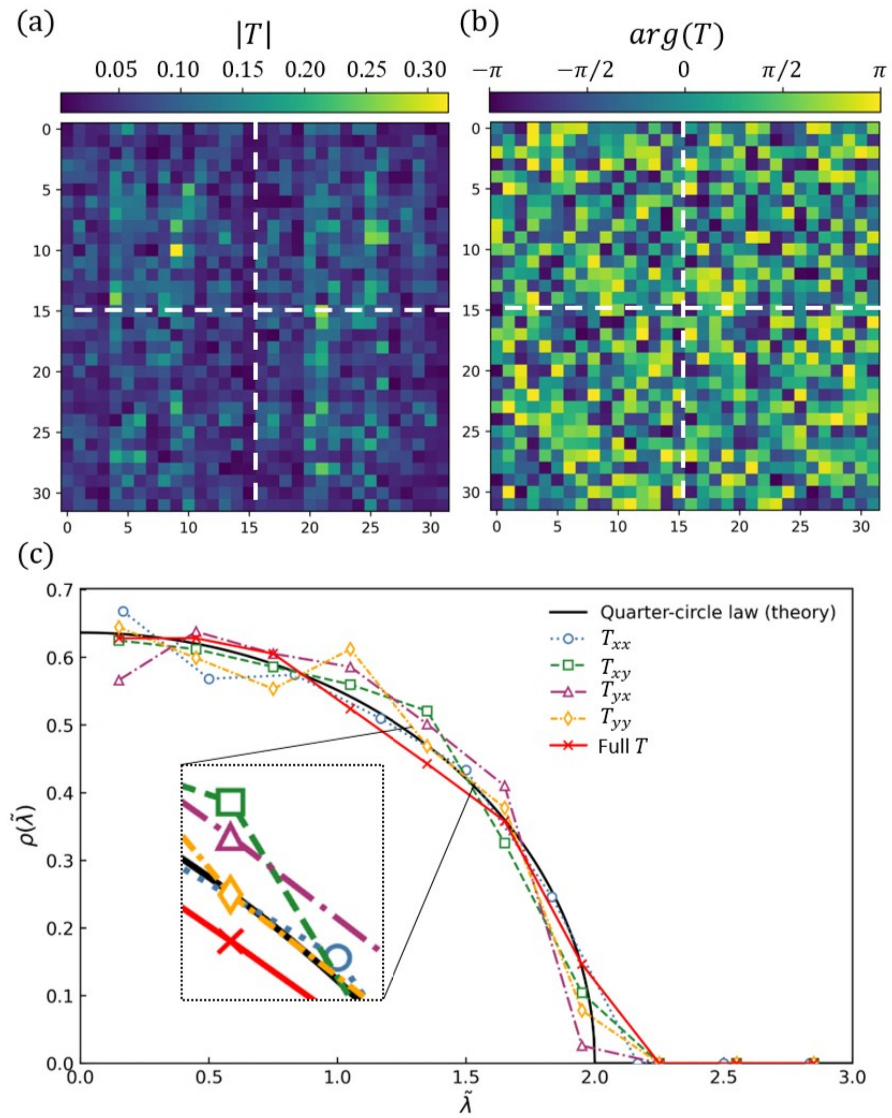

Figure 4. Dual-retardance retrieval ($\delta = \pi/2$, $3\pi/2$). (**a**) Magnitude and (**b**) phase of the retrieved $2m \times 2n$ VTM T. (**c**) Singular-value distributions of the four intrinsic blocks (T_{xx}, T_{xy}, T_{yx}, T_{yy}) and of the full matrix T after amplitude normalization and spatial decimation as in [19], shown together with the quarter-circle prediction for an i.i.d. complex random matrix [29]. In this case all curves closely follow the quarter-circle law, confirming that the second, linearly independent retardance removes the inter-block correlations seen in the single-retardance case. An enlarged view of a selected region is provided for better visibility.

The pipeline, comprising both VTM retrieval and input wavefront shaping, executes in under 30 s for sizes $n = m = 16$. For this configuration, the retrieval algorithm operates at an average rate of approximately 24 iterations per second, while the input-shaping neural network achieves around 1400 iterations per second. The optical setup remains sufficiently stable over this time interval, ensuring that no significant artifacts arise from temporal decorrelation effects. Naturally, as the input, output, and probe sizes increase, or as the convergence rate varies, the overall computational time of the pipeline correspondingly increases. In a more rigorous language, the VTM retrieval algorithm has $O(p \cdot k \cdot n \cdot (n+m))$ algorithmic time-complexity and the input shaping neural network has $O(p \cdot m \cdot n)$ time complexity, where p is the number of iterations for each algorithm. More details on the convergence speed of the retrieval algorithm can be found in Appendix D.

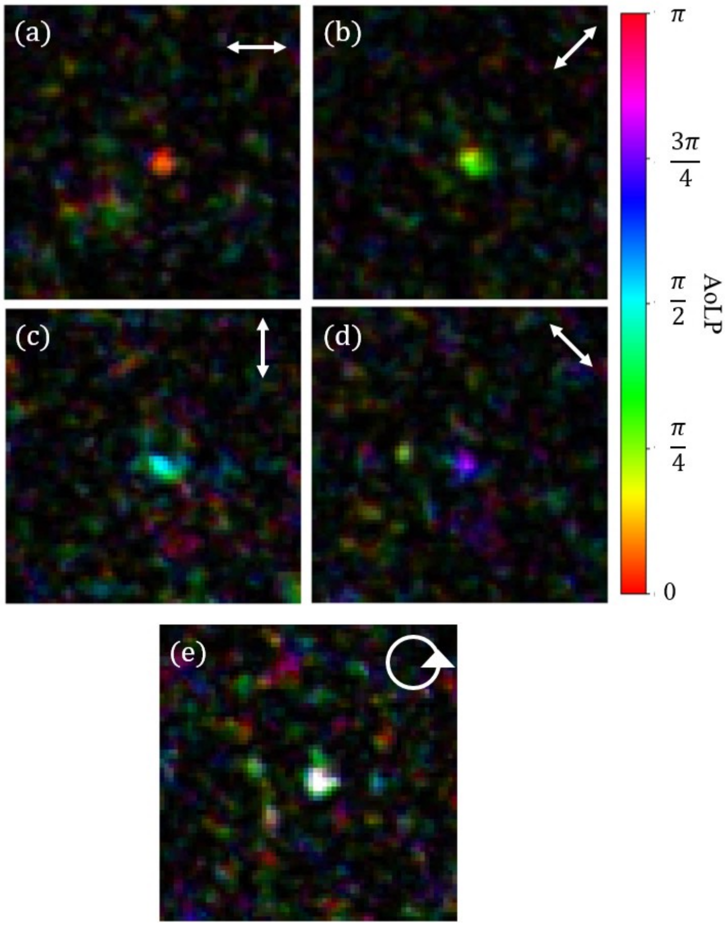

Figure 5. Polarization-resolved focusing using the retrieved VTM and a feed-forward controller. For each target polarization: (**a**) linear horizontal, (**b**) linear at 45°, (**c**) linear vertical, (**d**) linear at 135°, and (**e**) left circular, (arrows in the top-right corners show above-described polarization orientations) the network outputs a single SLM modulation pattern whose forward propagation through T produces a focus with the requested polarization state and spatial position. All panels show the AoLP derived from the Stokes parameters; for the left-circular target, the local AoLP is randomly distributed, resulting in an achromatic (white) focus. Across all cases, the focusing enhancement ranges between 7 and 10 times above the background. The mean polarization accuracy deviates by less than 1° with a standard deviation of about 5° within the focal region, and for the circular focus the DoLP is 0.1 ± 0.02.

5. Discussion

A further advantage of using the SLM followed by a programmable LCVR in a single-path geometry is that the same two-retardance strategy is not restricted to the linear (x, y) basis. In the results above we expressed the fields in linear components, so with a single LCVR setting we obtained an effective VTM whose four linear polarization channels were still coupled, and with two linearly independent LCVR settings, $\delta = \pi/2$ and $\delta = 3\pi/2$, we were able to separate them. The same idea can be applied in the right/left circular basis, simply by expressing both the input and the output fields in that basis. In that case, the LCVR at $\delta = 0$ and $\delta = \pi$ will produce two linearly independent illuminations in the circular basis and lead to a fully analogous situation: with a single retardance the VTM expressed in the circular (R, L) basis will show correlations between the four circular channels (RR, RL, LR, LL) because the two circular components are not fully independent, and with the second retardance those correlations can be removed and the four channels can be retrieved separately. This flexibility can be useful for analyses of scattering materials sensitive to either linear or circular polarization, such as aligned polymers, fibrous or anisotropic media, quartz, or cholesteric liquid crystals. Moreover, the scheme is not intrinsically limited to 532 nm: the same single-path strategy can, in principle, be transferred to other optical bands as long as phase/polarization control and polarization-resolved detection are available at the target wavelength.

6. Conclusions

We showed that a single-path SLM setup combined with full-Stokes detection and an adapted Gerchberg–Saxton update can recover a predictive vector transmission matrix from intensity-only data. With only one setting of the liquid-crystal retarder, the two polarization components of the input are not controlled independently, so the reconstructed matrix shows correlations between its polarization channels and its singular-value statistics depart from the ideal random-matrix behavior. When two linearly independent retarder settings are used, $\delta = \pi/2$ and $\delta = 3\pi/2$, this limitation is removed and the four polarization channels can be retrieved separately. In the experimental configuration with 16×16 input–output spatial modes, the retrieved VTM predicts test-speckle intensities with about 90% correlation and supports polarization-resolved focusing with an enhancement of up to $10\times$ over the background for horizontal, vertical, arbitrary linear, and circular states. The retrieval also showed stable convergence across repeated measurements, indicating that the scheme is robust to moderate experimental imperfections. Overall, the use of minimal hardware together with full-Stokes constraints provides an interferometer-free route to deterministic vectorial control and to the characterization of polarization transport in complex media.

Author Contributions: All authors contributed to the conceptualization, methodology, investigation, and writing of the manuscript. All authors have read and agreed to the published version of the manuscript.

Funding: This research was funded by the Higher Education and Science Committee of the Republic of Armenia, grant No. 22rl-060.

Institutional Review Board Statement: Not applicable.

Informed Consent Statement: Not applicable.

Data Availability Statement: Data supporting the reported results are available from the corresponding author upon reasonable request.

Acknowledgments: The authors acknowledge discussions within the PhotonicsAI Laboratory at Yerevan State University.

Conflicts of Interest: The authors declare no conflicts of interest.

Abbreviations

VTM	Vector transmission matrix
SLM	Spatial light modulator
FSPM	Full-Stokes polarimetry module
LCVR	Liquid-crystal variable retarder
QWP	Quarter-wave plate
AoLP	Angle of linear polarization
DoLP	Degree of linear polarization

Appendix A. Input Polarization Mapping by the LCVR and Linear Independence of Two Settings

We start from right–circular polarization at the SLM,

$$E_{\mathrm{SLM,in}} = \frac{E_0}{\sqrt{2}}\begin{bmatrix}1\\-i\end{bmatrix},$$

and x–only phase modulation by the SLM,

$$E_{\mathrm{after\,SLM}} = \frac{E_0}{\sqrt{2}}\begin{bmatrix}e^{i\phi(\mathbf{r})}\\-i\end{bmatrix}.$$

A linear retarder of retardance δ with fast axis fixed at -45° has Jones matrix

$$J_{-45}(\delta) = R(-\pi/4)\begin{bmatrix}1 & 0\\0 & e^{i\delta}\end{bmatrix}R(\pi/4) = \frac{1}{2}\begin{bmatrix}1+e^{i\delta} & 1-e^{i\delta}\\1-e^{i\delta} & 1+e^{i\delta}\end{bmatrix},$$

with $R(\cdot)$ the real rotation matrix. The field at the sample entrance is then

$$\begin{bmatrix}E_{\mathrm{in},x}\\E_{\mathrm{in},y}\end{bmatrix} = \frac{E_0}{\sqrt{2}}J_{-45}(\delta)\begin{bmatrix}e^{i\phi(\mathbf{r})}\\-i\end{bmatrix} = \frac{E_0}{2\sqrt{2}}\begin{bmatrix}(1+e^{i\delta})\,e^{i\phi} - i(1-e^{i\delta})\\(1-e^{i\delta})\,e^{i\phi} - i(1+e^{i\delta})\end{bmatrix}. \tag{A1}$$

For the two experimental retardances, $\delta = \pi/2$ and $3\pi/2$ (corresponding to $e^{i\delta} = \pm i$), Equation (A1) yields

$$E_{\mathrm{in},x} = \frac{E_0}{2\sqrt{2}}\,(1\pm i)\,\big(e^{i\phi}\mp 1\big), \qquad E_{\mathrm{in},y} = \frac{E_0}{2\sqrt{2}}\,(1\mp i)\,\big(e^{i\phi}\pm 1\big).$$

In both cases, the ratio $E_{\mathrm{in},x}/E_{\mathrm{in},y}$ is purely real ($-\tan(\phi/2)$ for $+$ and $-\cot(\phi/2)$ for $-$), indicating that the input field is everywhere linearly polarized ($S_3 = 0$). The two settings thus produce spatially varying linear polarization patterns with opposite AoLP, i.e., the AoLP map changes sign between the two retardances.

In summary, both retardances produce spatially varying linear polarization from the same SLM phase pattern; only the AoLP map changes sign between the two settings. This pair of linearly independent polarization modulations is what we exploit later to decouple the intrinsic VTM blocks.

Appendix B. Derivation of Input Coupling (Single Retardance) and Full VTM Recovery with Two Retardance Settings

Starting from Equation (A1), we obtain the exact pixelwise affine relation between the orthogonal components:

$$E_{\mathrm{in},y} = \alpha(\delta)\,E_{\mathrm{in},x} + g(\delta), \qquad \alpha(\delta) = \frac{1-e^{i\delta}}{1+e^{i\delta}}, \qquad g(\delta) = -\,i\,\frac{\sqrt{2}\,E_0\,e^{i\delta}}{1+e^{i\delta}}. \tag{A2}$$

Vectorizing over all n input pixels,

$$\mathbf{E}_{\mathrm{in},y} = \alpha\,\mathbf{E}_{\mathrm{in},x} + \mathbf{g}, \qquad \mathbf{g} := g\,\mathbf{1}_n \in \mathbb{C}^n.$$

Let the vector transmission matrix be

$$T = \begin{bmatrix}T_{xx} & T_{xy}\\T_{yx} & T_{yy}\end{bmatrix} \in \mathbb{C}^{2m\times 2n}, \qquad \begin{bmatrix}\mathbf{E}_{\mathrm{out},x}\\\mathbf{E}_{\mathrm{out},y}\end{bmatrix} = T\begin{bmatrix}\mathbf{E}_{\mathrm{in},x}\\\mathbf{E}_{\mathrm{in},y}\end{bmatrix}.$$

Using Equation (A2) and writing $\mathbf{U} := \mathbf{E}_{\text{in},x} \in \mathbb{C}^n$, one obtains the single-retardance input–output relation (with intercepts):

$$\begin{bmatrix} \mathbf{E}_{\text{out},x} \\ \mathbf{E}_{\text{out},y} \end{bmatrix} = \underbrace{\begin{bmatrix} T_{xx} + \alpha T_{xy} \\ T_{yx} + \alpha T_{yy} \end{bmatrix}}_{T^{(\alpha)} \in \mathbb{C}^{2m \times n}} \mathbf{U} + \underbrace{\begin{bmatrix} T_{xy}\,\mathbf{g} \\ T_{yy}\,\mathbf{g} \end{bmatrix}}_{\mathbf{B} \in \mathbb{C}^{2m}}. \tag{A3}$$

Equivalently, with

$$A := T_{xx} + \alpha T_{xy}, \quad C := T_{yx} + \alpha T_{yy}, \quad \mathbf{b} := T_{xy}\,\mathbf{g}, \quad \mathbf{d} := T_{yy}\,\mathbf{g}, \tag{A4}$$

Equation (A3) reads

$$\begin{bmatrix} \mathbf{E}_{\text{out},x} \\ \mathbf{E}_{\text{out},y} \end{bmatrix} = \begin{bmatrix} A \\ C \end{bmatrix} \mathbf{U} + \begin{bmatrix} \mathbf{b} \\ \mathbf{d} \end{bmatrix}. \tag{A5}$$

Thus, for a single retardance one identifies the effective mapping $T^{(\alpha)} = [A; C]$ together with constant offsets $(\mathbf{b}, \mathbf{d})$; the four intrinsic blocks are not separately identifiable.

With two distinct retardances $\delta_1 \neq \delta_2$ (thus $\alpha_1 \neq \alpha_2$), we estimate $(A_1, \mathbf{b}_1)$ and $(C_1, \mathbf{d}_1)$ at δ_1, and $(A_2, \mathbf{b}_2)$ and $(C_2, \mathbf{d}_2)$ at δ_2. The intrinsic blocks then follow, rowwise, from Equation (A4)

$$T_{xy} = \frac{A_2 - A_1}{\alpha_2 - \alpha_1}, \quad T_{xx} = \frac{\alpha_2 A_1 - \alpha_1 A_2}{\alpha_2 - \alpha_1}, \quad T_{yy} = \frac{C_2 - C_1}{\alpha_2 - \alpha_1}, \quad T_{yx} = \frac{\alpha_2 C_1 - \alpha_1 C_2}{\alpha_2 - \alpha_1}. \tag{A6}$$

From Equation (A2): $\alpha_1 = -i$, $\alpha_2 = +i$, $g_1 = \frac{E_0}{\sqrt{2}}(1 - i)$, $g_2 = -\frac{E_0}{\sqrt{2}}(1 + i)$, so $|\alpha_2 - \alpha_1| = 2$ and $|g_1| = |g_2| = E_0$. Equation (A6) simplifies to

$$T_{xy} = \frac{A_2 - A_1}{2i}, \qquad T_{xx} = \frac{A_1 + A_2}{2}, \qquad T_{yy} = \frac{C_2 - C_1}{2i}, \qquad T_{yx} = \frac{C_1 + C_2}{2}. \tag{A7}$$

Appendix C. Optical Components

The following table provides details of the principal optical elements used in the single-path scattering experiment (Figure 1).

The measured electro-optical response of the LCVR, provided by the manufacturer for our specific device, is shown in Figure A1. The sdata represent the dependence of the optical retardance on the applied voltage at a wavelength of 531.7 nm. As the voltage increases, the liquid crystal molecules align progressively with the applied electric field, reducing the effective birefringence and thus the optical retardance. This characterization was used as a reference for the calibration of our system and ensures accurate control of the required retardance states, specifically 0, $\pi/4$, $\pi/2$, and $3\pi/4$.

Building upon the characterization of the LCVR described above, we next verified the performance of the FSPM, which consists of the LCVR and a polarization-sensitive camera. To ensure correct operation and calibration, we measured several well-defined input polarization states. Starting from our vertically polarized 532 nm laser beam, the desired states were prepared by inserting a half-wave plate (for horizontal, vertical, and $\pm 45^\circ$ linear polarization) and a quarter-wave plate (for right- and left-handed circular polarization) and rotating them to the corresponding angles. For each input state, the four analyzer images were recorded, the Stokes parameters S_0–S_3 were computed, and then the normalized Stokes parameters $s_i = S_i/S_0$ ($i = 1, 2, 3$) were obtained for comparison with the ideal values. The results are summarized in Table A2.

Table A1. Detailed specifications of main optical components.

Component	Details
Laser	Manufacturer: Changchun New Industries Optoelectronics Technology Model: MSL-U-532, Single Lognitudinal Mode Laser Key Specifications: Wavelength: 532 nm Polarization Ratio: >100:1, Vertical Max Output power: 1 W M^2 factor: < 1.2
SLM	Manufacturer: Meadowlark Optics Model: HSP1K, Spatial Light Modulator Key Specifications: Type: Liquid Crystal on Silicon (LCoS) Optical Axis Direction: Horizontal Color Coding: Raw 8 bit Resolution: 1024×1024 Pixel pitch: 17 × 17 µm
LCVR	Manufacturer: Meadowlark Optics Model: D5020-HS, HLC-200-VIS, Liquid Crystal Variable Retarder Key Specifications: Fundamental Drive Waveform: 2 kHz AC square wave Retardance: −50–425 nm Voltage Range: 0–20 Vrms Beam Deviation: ≤2 arc min
Polarization Camera	Manufacturer: Alkeria Model: Celera C5S-MP Key Specifications: Sensor Type: Mono Polarized Sensor Model: SONY Pregius IMX250MZR Sensor resolution: 2464 × 2056 Sensor technology: CMOS, global shutter Polarization Configuration: On-pixel filters in a 2 × 2 calculation unit with orientations of 0°, 45°, 90°, and 135°.

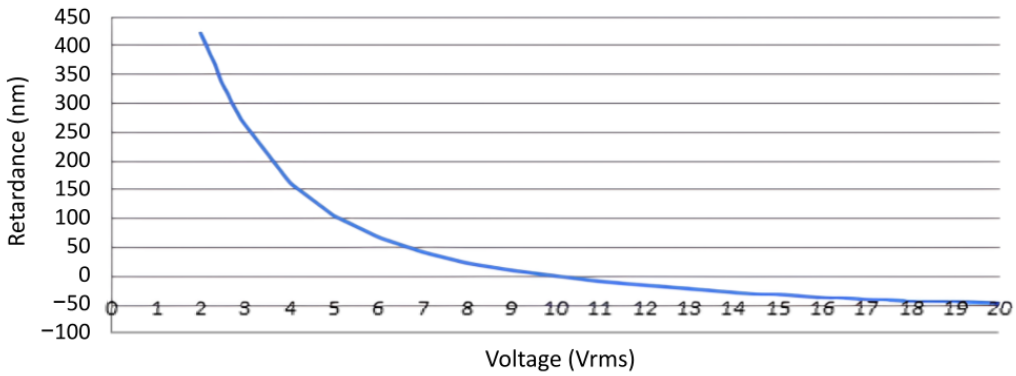

Figure A1. Retardance as a function of applied voltage for the LCVR at 531.7 nm. Increasing voltage reduces retardance due to electric-field-induced alignment of liquid crystal molecules and corresponding decrease in birefringence.

Table A2. Measured normalized Stokes parameters (s_1, s_2, s_3) for different input polarization states. The standard deviation of all measurements is $\approx$0.02.

Polarization	s_1	s_2	s_3
H	0.989	−0.028	−0.014
V	−0.999	0.010	0.034
45°	0.049	0.998	0.014
−45°	−0.042	−0.994	−0.094
R	−0.010	0.000	0.999
L	0.035	−0.179	−0.983

Appendix D. Statistical Analysis of Retrieval Algorithm

To assess the repeatability and statistical behavior of the proposed retrieval algorithm, we performed 64 independent experiments using identical sets of input fields. The scattering medium slowly evolved between measurements, resulting in distinct transmission matrices for each trial. The experimental conditions and acquisition parameters were kept constant. The experiments were conducted for $n = m = 16$ size. This series of measurements enables a statistical characterization of the algorithm's performance over multiple realizations rather than a single fixed configuration.

Figure A2a shows the distribution of correlations computed between the calculated ()based on the retrieved VTM) and experimentally measured output fields across all repetitions. The results indicated that on average we get 0.9025 ± 0.00067 output correlation. The imperfect correlations are the results of imperfections in the optical elements, subtle misalignments, and other external influences.

In addition, Figure A2b summarizes the distribution of convergence speeds, quantified by the iteration index at which the algorithm first satisfies the convergence criterion described in Section 3. In each case the optimization was run until either the convergence criterion was met or a maximum number of 500 iterations was completed. In all repeated runs the convergence criterion was met before reaching the maximum iteration limit. On average the algorithm converges in 257 ± 8 iterations for the given configuration. As it is described in [26], the convergence process depends on the number of the input modes and the number of the input patterns used for the optimization, as well as the initialization. So, for different configurations the convergence speed varies.

Together, these observations provide useful statistical insight into the repeatability and internal dynamics of the retrieval process, supporting its reliability for further experimental and comparative studies.

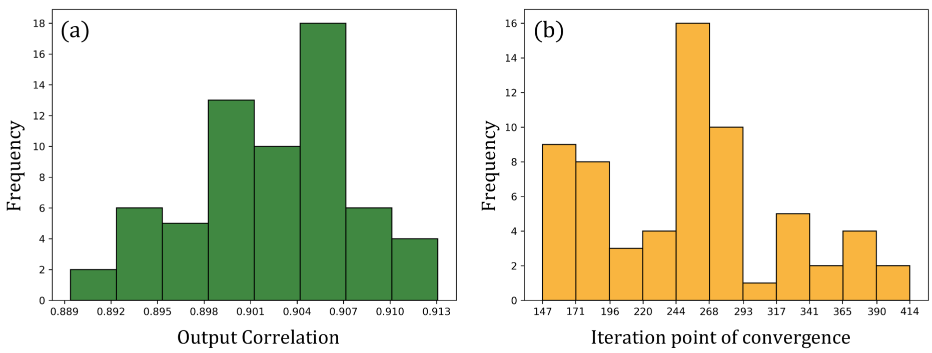

Figure A2. Statistical characterization of the retrieval algorithm: (**a**) output correlations and (**b**) convergence speed across 64 repeated experiments.

References

1. Bicout, D.; Brosseau, C.; Martinez, A.S.; Schmitt, J.M. Depolarization of multiply scattered waves by spherical diffusers: Influence of the size parameter. *Phys. Rev. E* **1994**, *49*, 1767. [CrossRef] [PubMed]
2. Xu, M.; Alfano, R.R. Random walk of polarized light in turbid media. *Phys. Rev. Lett.* **2005**, *95*, 213901. [CrossRef]
3. Brasselet, S. Polarization-resolved nonlinear microscopy: Application to structural molecular and biological imaging. *Adv. Opt. Photonics* **2011**, *3*, 205. [CrossRef]
4. Rotter, S.; Gigan, S. Light fields in complex media: Mesoscopic scattering meets wave control. *Rev. Mod. Phys.* **2017**, *89*, 015005. [CrossRef]
5. Gigan, S.; Katz, O.; De Aguiar, H.B.; Andresen, E.R.; Aubry, A.; Bertolotti, J.; Bossy, E.; Bouchet, D.; Brake, J.; Brasselet, S.; et al. Roadmap on wavefront shaping and deep imaging in complex media. *J. Phys. Photonics* **2022**, *4*, 042501. [CrossRef]
6. Yu, Z.; Li, H.; Zhong, T.; Park, J.H.; Cheng, S.; Woo, C.M.; Zhao, Q.; Yao, J.; Zhou, Y.; Huang, X.; et al. Wavefront shaping: A versatile tool to conquer multiple scattering in multidisciplinary fields. *Innovation* **2022**, *3*, 100292. [CrossRef]
7. Rosen, J.; Alford, S.; Allan, B.; Anand, V.; Arnon, S.; Arockiaraj, F.G.; Art, J.; Bai, B.; Balasubramaniam, G.M.; Birnbaum, T.; et al. Roadmap on computational methods in optical imaging and holography. *Appl. Phys. B* **2024**, *130*, 166. [CrossRef]
8. Shen, L.; Zhang, L.; Qi, P.; Zhang, X.; Li, X.; Huang, Y.; Zhao, Y.; Hu, H. Polarimetric binocular three-dimensional imaging in turbid water with multi-feature self-supervised learning. *PhotoniX* **2025**, *6*, 24. [CrossRef]
9. Mosk, A.P.; Lagendijk, A.; Lerosey, G.; Fink, M. Controlling waves in disordered media: Current state of the art. *Nat. Photonics* **2012**, *6*, 283–292. [CrossRef]
10. Freund, I. Correlation functions of random wave fields. *Phys. A Stat. Mech. Its Appl.* **1990**, *168*, 49–62. [CrossRef]
11. Webster, M.A.; Gerke, T.D.; Weiner, A.M.; Webb, K.J. Polarization-sensitive optical coherence tomography for tissue imaging. *Opt. Lett.* **2004**, *29*, 1491–1493. [CrossRef]
12. Tripathi, S.; Paxman, R.; Bifano, T.; Toussaint, K.C., Jr. Vector transmission matrix for the polarization behavior of light propagation in highly scattering media. *Opt. Express* **2012**, *20*, 16067–16076. [CrossRef]
13. Vellekoop, I.M.; Mosk, A.P. Focusing light through an opaque scattering medium. *Opt. Lett.* **2007**, *32*, 2309–2311. [PubMed]
14. Vellekoop, I.M.; Lagendijk, A.; Mosk, A. Exploiting disorder for perfect focusing. *Nat. Photonics* **2010**, *4*, 320–322. [CrossRef]
15. Katz, O.; Small, E.; Bromberg, Y.; Silberberg, Y. Controlling light in time and space through a complex medium. *Nat. Photonics* **2011**, *5*, 372–377. [CrossRef]
16. Aulbach, J.; Gjonaj, B.; Johnson, P.M.; Mosk, A.P.; Lagendijk, A. Control of the spectral intensity of light transmitted through a disordered medium. *Phys. Rev. Lett.* **2011**, *106*, 103901. [PubMed]
17. McCabe, D.J.; Tajalli, A.; Austin, D.R.; Bondareff, P.; Walmsley, I.A.; Gigan, S.; Chatel, B. Spatio-temporal focusing of light through a multiple scattering medium. *Nat. Commun.* **2011**, *2*, 447.
18. Small, E.; Katz, O.; Guan, Y.; Silberberg, Y. Focusing light through a scattering medium with a digital mirror device. *Opt. Lett.* **2012**, *37*, 3429–3431. [CrossRef]
19. Popoff, S.M.; Lerosey, G.; Carminati, R.; Fink, M.; Boccara, A.C.; Gigan, S. Measuring the Transmission Matrix in Optics: An Approach to the Study and Control of Light Propagation in Disordered Media. *Phys. Rev. Lett.* **2010**, *104*, 100601. [CrossRef]
20. Guan, Y.; Katz, O.; Small, E.; Zhou, J.; Silberberg, Y. Polarization control of multiply scattered light through random media by wavefront shaping. *Opt. Lett.* **2012**, *37*, 4663–4665. [CrossRef]
21. Galstian, T.; Gauvin, F.; Larochelle, P. Local Electrooptic Enhancement of the Degree of Linear Polarization of Coherently Scattered Light. *Opt. Commun.* **2025**, *596*, 132412. [CrossRef]
22. Park, J.; Park, J.H.; Yu, H.; Park, Y. Focusing through turbid media by polarization modulation. *Opt. Lett.* **2015**, *40*, 1667–1670. [CrossRef]
23. Tripathi, S. Optical Polarization Control in Free Space and Through Random Media Using Wavefront Shaping. Ph.D. Thesis, University of Illinois at Urbana-Champaign, Champaign, IL, USA, 2014.
24. Xiong, W.; Hsu, C.W.; Bromberg, Y.; Antonio-Lopez, J.E.; Amezcua Correa, R.; Cao, H. Complete polarization control in multimode fibers with polarization and mode coupling. *Light Sci. Appl.* **2018**, *7*, 54. [CrossRef]
25. de Aguiar, H.B.; Gigan, S.; Brasselet, S. Polarization recovery through scattering media. *Sci. Adv.* **2017**, *3*, e1600743. [CrossRef]
26. Huang, G.; Wu, D.; Luo, J.; Lu, L.; Li, F.; Shen, Y.; Li, Z. Generalizing the Gerchberg–Saxton algorithm for retrieving complex optical transmission matrices. *Photonics Res.* **2020**, *9*, 34–42. [CrossRef]
27. Vector Transmission Matrix Retrieval and Input Shaping for Focusing. 2025. Available online: https://github.com/photonics-ai-lab/vector-tm-retrieval-and-input-shaping (accessed on 12 November 2025).
28. Šverko, Z.; Vrankić, M.; Vlahinić, S.; Rogelj, P. Complex Pearson correlation coefficient for EEG connectivity analysis. *Sensors* **2022**, *22*, 1477. [CrossRef] [PubMed]
29. Marčenko, V.A.; Pastur, L.A. Distribution of eigenvalues for some sets of random matrices. *Math. USSR-Sb.* **1967**, *1*, 457. [CrossRef]

30. Drémeau, A.; Liutkus, A.; Martina, D.; Katz, O.; Schülke, C.; Krzakala, F.; Gigan, S.; Daudet, L. Reference-less measurement of the transmission matrix of a highly scattering material using a DMD and phase retrieval techniques. *Opt. Express* **2015**, *23*, 11898–11911. [CrossRef]
31. Zhao, T.; Ourselin, S.; Vercauteren, T.; Xia, W. Seeing through multimode fibers with real-valued intensity transmission matrices. *Opt. Express* **2020**, *28*, 20978–20991. [CrossRef] [PubMed]